Research Article

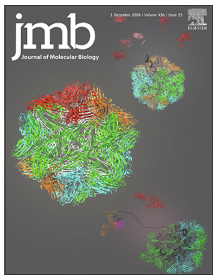

Disruption of CAD Oligomerization by Pathogenic Variants

Francisco Del Caño-Ochoa [1,*], Lobna Ramadane-Morchadi [2], Lluís Eixerés [1], María Moreno-Morcillo [3], Rafael Fernández-Leiro [3], and Santiago Ramón-Maiques [1,4,5,*]

*1 - **Structure of Macromolecular Targets Unit,** Instituto de Biomedicina de Valencia (IBV), CSIC, Eduardo Primo Yúfera, 3, 46012 Valencia, Spain*
*2 - **Molecular Oncology Laboratory,** Hospital Clínico San Carlos, IdISSC (Instituto de Investigación Sanitaria del Hospital Clínico San Carlos), Prof Marín Lagos, S/N, 28040 Moncloa-Aravaca, Madrid, Spain*
*3 - **Genome Integrity and Structural Biology Group,** Spanish National Cancer Research Centre (CNIO), Melchor Fernández Almagro, 3, 28029 Madrid, Spain*
*4 - **Group CB06/07/0077 Centro de Investigación Biomédica en Red de Enfermedades Raras,** CIBERER-ISCIII, Monforte de Lemos 3-5, 28029 Madrid, Spain*
*5 - **Valencia Biomedical Research Foundation,** Centro de Investigación Príncipe Felipe (CIPF) – Associated Unit to the Instituto de Biomedicina de Valencia (IBV), Eduardo Primo Yúfera, 3, 46012 Valencia, Spain*

Correspondence to Francisco Del Caño-Ochoa and Santiago Ramón-Maiques: Instituto de Biomedicina de Valencia (IBV), CSIC, Eduardo Primo Yúfera, 3, Valencia 46012, Spain (S. Ramón-Maiques), Instituto de Biomedicina de Valencia (IBV), CSIC, Eduardo Primo Yúfera, 3, Valencia, 46012, Spain (F. Del Caño-Ochoa).
fdelcano@ibv.csic.es (F. Del Caño-Ochoa), sramon@ibv.csic.es (S. Ramón-Maiques)
https://doi.org/10.1016/j.jmb.2024.168832
Edited by Georg Schulz

Abstract

CAD, the multi-enzymatic protein essential for initiating the *de novo* biosynthesis of pyrimidine nucleotides, forms large hexamers whose structure and function are not fully understood. Defects in CAD cause a severe neurometabolic disorder that is challenging to diagnose. We developed a cellular functional assay to identify defective CAD variants, and in this study, we characterized five pathogenic missense mutations in CAD's dihydroorotase (DHO) and aspartate transcarbamoylase (ATC) domains. All mutations impaired enzymatic activities, with two notably disrupting the formation of DHO dimers and ATC trimers. Combining crystal structures and AlphaFold predictions, we modeled the hexameric CAD complex, highlighting the central role of the DHO and ATC domains in its assembly. Our findings provide insight into CAD's stability, function, and organization, revealing that correct oligomerization of CAD into a supramolecular complex is required for its function in nucleotide synthesis and that mutations affecting this assembly are potentially pathogenic.

Introduction

Genome-wide sequencing is critical for identifying causal mutations in inherited metabolic diseases, but interpreting the impact of individual genomic alterations poses significant challenges. Many genetic missense variants have uncertain effects and require functional assays and detailed

characterization of the target proteins to assess their clinical relevance and to understand the dysfunction mechanisms of the "diseased protein".

Recent studies have identified defects in CAD, a multi-enzymatic protein initiating *de novo* pyrimidine nucleotide biosynthesis,[1–3] as the cause of an autosomal recessive neurometabolic disorder (OMIM #616457) that manifests in newborns and young children.[4,5] The disease is characterized by early-onset refractory epilepsy, developmental delay, severe developmental regression, and anemia.[6] The untreated disease is often fatal, but patients show remarkable improvement with oral supplements of uridine, which fuel pyrimidine nucleotide synthesis via a CAD-independent salvage pathway.[7–15] However, diagnosis is challenging due to symptoms overlapping with other conditions, the absence of a biomarker, and the observation of >2,400 missense CAD variants in the general population (gnomAD v4.0, ENSG00000084774). Our limited understanding of CAD complicates the prediction of whether a clinical missense variant is pathogenic or benign.

CAD is a poorly understood protein of 2,225 amino acids, formed by the fusion of four enzymatic domains, each catalyzing an initial step in *de novo* pyrimidine synthesis (Figure 1A).[16,2,3] This large protein further oligomerizes into hexamers of ~1.5 MDa, nearly half the size of a ribosome.[2,17] Although the structure of the hexamer has not been described, our group determined the crystal structures of CAD's isolated dihydroorotase (DHO) and aspartate transcarbamoylase (ATC) domains, showing that they assemble into dimers and trimers, respectively.[18–21] Combined with mutagenesis analysis, these findings support a model in which CAD trimers, linked by the ATC domains, further dimerize through the DHO domains, forming hexamers or "dimer of trimers".[22,23] However, the architecture and functional implications of this mega-enzyme remain uncharacterized.

To overcome the challenges of evaluating the pathogenicity of missense CAD variants, we developed a functional assay using a CAD-knockout (KO) human cell line that can only grow in media supplemented with uridine.[24] We transiently transfect these cells with a CAD cDNA containing the specific patient variant and monitor proliferation over a week in uridine-free conditions. This method identifies mutations that disrupt CAD activity and impede proliferation, indicating pathogenicity, while normal cell growth suggests that the variant is likely benign. In previous studies, we used this proliferation assay to identify for the first time or confirm the pathogenicity of 34 missense variants, helping diagnose CAD-deficient patients worldwide.[24,25]

At the same time, identifying pathogenic mutations serves as a key to unlocking our understanding of CAD, as they point to crucial elements for the protein's stability, function, and organization. Intriguingly, the largest number of deleterious changes (35%) accumulated within CAD's DHO domain, representing only a small portion (1/6) of the entire protein. Thus, we produced and characterized eight DHO pathogenic variants to study the importance of this domain in CAD function. All mutations except for one were shown to impede substrate binding or decrease protein stability[25]. One mutation, R1785C, was proposed to possibly alter interactions with the CPS-2 domain given the short three-residue linker between the two domains.

In this study, we further interrogate the functioning of CAD by studying five confirmed pathogenic mutations: three in the DHO domain and two in the ATC domain (Figure 1A).[25] Our findings reveal that although all mutations have a detrimental effect on enzymatic activity, two of them strongly impair the formation of the DHO dimers and ATC trimers. Combining AlphaFold predictions with crystal structure information, we constructed a model of the CAD hexamer that highlights the central role of the DHO and ATC in the architecture of the particle. This study marks the discovery of pathogenic changes that affect CAD oligomerization, underscoring the critical role of assembling into a functional supramolecular complex for the proper function in the nucleotide synthesis pathway.

Materials and Methods

Protein production

The cDNA encoding the human DHO domain (aa 1,456–1,846) or the ATC domain (aa 1,917–2,225) in mutated CAD constructs was PCR amplified and inserted into pOPIN-M (Oxford Protein Production Facility) by IVA cloning.[26] DHO wild-type (WT) and mutants were expressed in HEK293 cells and purified as described.[18,19,27] Briefly, HEK293S-GnTI cells in suspension were transiently transfected using polyethylenimine, grown for 2 days and frozen at −80 °C until purification. Cells were lysed in buffer A (20 mM Tris–HCl, pH 8, 0.5 M NaCl, 10 mM imidazole, 5% glycerol, and 2 mM β-mercaptoethanol) with 2 mM phenylmethanesulfonyl fluoride using a Dounce homogenizer and brief sonication. Following clarification by centrifugation, the protein was purified using a HisTrap FF column (Cytiva) and dialyzed against buffer A containing 30 mM imidazole and treated with GST-tagged PreScission protease to cleave the N-terminal His_6-MBP tag. The sample was reloaded onto a HisTrap column connected to a GSTrap FF column (Cytiva) that retained non-cleaved protein, His6-MBP tag, and protease. The DHO in the column flowthrough was concentrated by ultrafiltration and purified by size exclusion chromatography (SEC) on Superdex 200 10/300 GL or HiLoad Superdex 200 pg columns (Cytiva) equilibrated in buffer GF (20 mM Tris, pH 8, 0.15 M NaCl, 20 μM $ZnSO_4$, and 0.2 mM TCEP). The final sample was

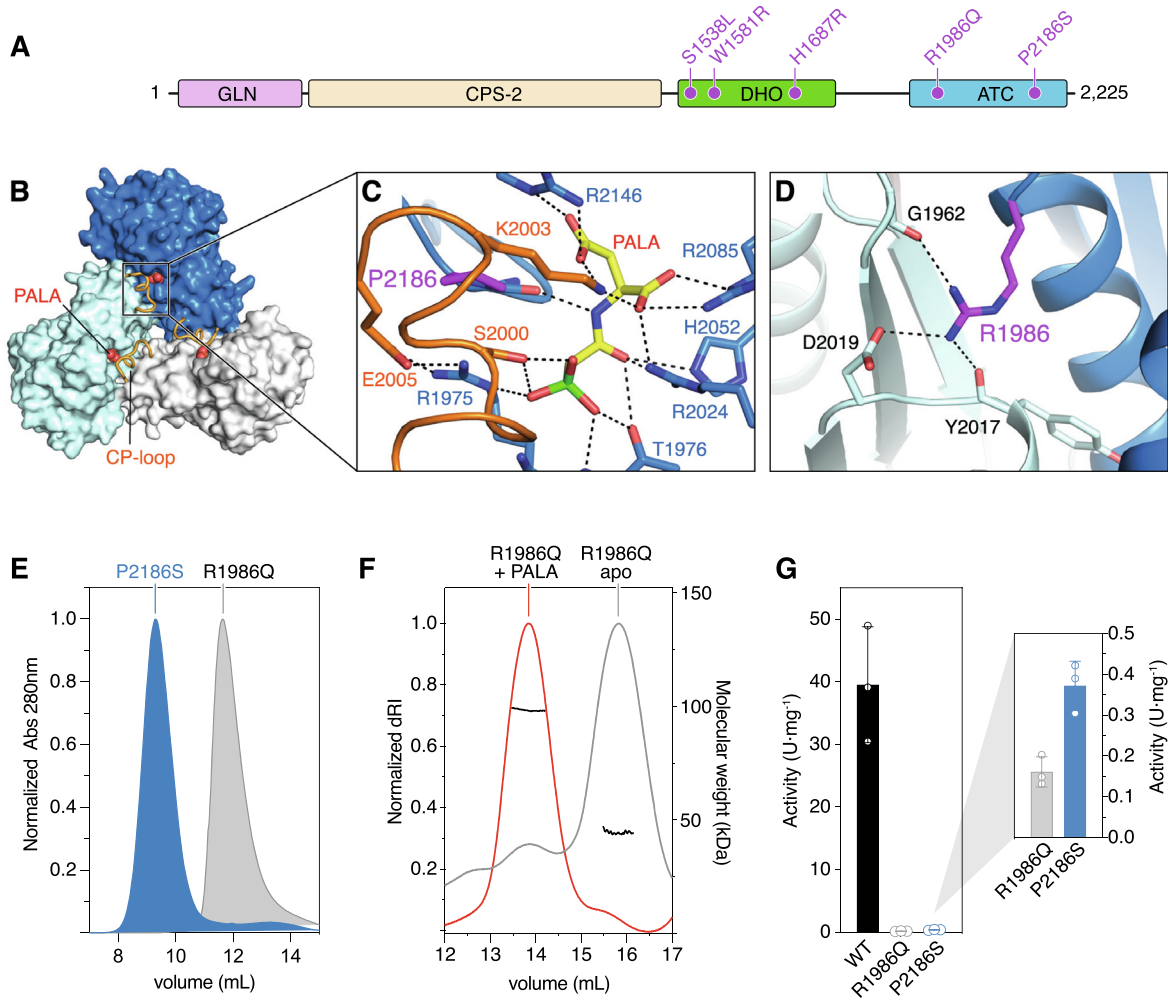

Figure 1. Pathogenic variants in CAD's ATC domain. A. Scheme of CAD protein with the four enzymatic domains represented by boxes. Pathogenic variants in the DHO and ATC domains are indicated in magenta. **B.** Surface representation of CAD's ATC homotrimer with each subunit in a different color. The CP-loop is represented in orange cartoon, and PALA as spheres. **C.** Detail of PALA binding in the active site and the mutated P2186 depicted in magenta. Dashed lines represent electrostatic interactions. **D.** Detail of the intersubunit interactions between the mutated residue R1986 and the neighboring subunit. **E.** SEC elution of ATC mutants P2186S and R1986Q indicate the formation of trimers and monomers, respectively. **F.** SEC-MALS analysis shows that PALA binding favors the assembly of R1986Q into trimers (98.4 ± 0.4 kDa), while the apo protein elutes as a monomer (39.5 ± 0.7 kDa). **G.** Enzymatic activity of WT and ATC mutants shown in scattered plot with three independent measurements. Error bars indicate standard deviation. Activity units (U) are nmol of carbamoyl aspartate per min.

concentrated as before and quantified by Bradford. Protein purification was monitored by SDS-PAGE. The production of mutants DHO-W1581R and DHO-H1687R was repeated twice in parallel with WT, consistently yielding lower amounts compared to WT and other DHO mutants.

ATC WT and mutants were expressed in bacteria and purified as previously reported,[20] with mutant yields comparable to WT.

Enzymatic assays

DHO catalyzes a reversible reaction that is pH-dependent.[28] Enzymatic activity was assayed spectrophotometrically following the production of dihydroorotate by absorbance at 230 nm at the favorable acidic pH and at 25 °C.[18] Reactions were carried out in a final volume of 100 μl containing 50 mM sodium phosphate pH 5.7, 150 mM NaCl, 20 μM $ZnSO_4$, 0.1 mg·ml^{-1} of bovine serum albumin (BSA; Sigma), and 5 mM carbamoyl aspartate (Ca-Asp; Sigma). Protein concentrations were 0.25 μM for the WT and were increased to 2.5–3 μM for the mutants. The reaction was triggered by adding Ca-Asp to a mix with the enzyme pre-incubated for 5 min at 25 °C.

ATC activity was assayed by a colorimetric method that quantifies the production of Ca-Asp.[20,29] Reactions were carried out in 50 mM Tris-acetate pH 8.3 and 0.1 mg·ml^{-1} BSA in a final

volume of 100 μl. Protein was pre-incubated with aspartate for 10 min by floating the tube in a water bath at 25 °C. The reaction was triggered by adding 5 mM carbamoyl phosphate (Sigma) and stopped at different times with 250 μl of color mix solution. The samples were boiled at 95 °C for 15 min and kept in the dark for 30 min before measuring the absorbance at 450 nm. Data analysis was performed with GraphPad Prism.

Differential scanning fluorimetry (DSF)

Protein stability was measured in triplicates by differential scanning fluorometry[30] using a CFX Opus 96 Real-Time PCR System (BioRad) in a 96-well reaction plate with 20 μl sample, containing 5 μM protein in GF buffer (20 mM Tris-HCl pH 7, 0.15 M NaCl and 2 mM DTT), 20x SYPRO Orange (Invitrogen) with or without 2 mM 5-fluoroorotate (FOA; Sigma). Fluorescence changes were monitored every 1 °C in a temperature ramp from 20 to 95 °C using the extrinsic fluorescence of SYPRO Orange ($\lambda_{excitation}$ = 465 nm, $\lambda_{emission}$ = 580 nm). Curves were normalized, and the melting temperature (T_m) was determined as the midpoint of the unfolding transition. Data were analyzed with GraphPad.

Crystallization and structure determination

Crystals of the mutated DHO alone or in the presence of 4 mM of Ca-Asp were obtained as reported.[18,19,27] Optimal crystallization conditions consisted of 2–3 mg·ml^{-1} of protein in GF buffer, 2–3 M sodium formate, and 0.1 M HEPES pH 6.5–7.5 as the mother liquor. Crystals were cryoprotected with 20% glycerol and flash-frozen. X-ray diffraction datasets were collected at XALOC (ALBA, Barcelona) and ID23-2 (ESRF, Grenoble). Data processing and scaling were performed automatically with autoPROC.[31,32] Crystallographic phases were obtained by molecular replacement with PHASER[33] and the WT DHO structure (PDB 4C6C and 4C6J) as the search model. Protein models were traced with COOT[34] and refined with PHENIX[35] or Refmac5.[36,37]

SEC coupled to multi-angle light scattering (SEC-MALS) analysis

400 μl of purified protein at 2 mg·ml^{-1} was fractionated on a Superdex 200 10/300 column (Cytiva) equilibrated in GF buffer, using an AKTA purifier (Cytiva). The eluted samples were characterized by in-line measurement of the refractive index and multi-angle light scattering using Optilab T-rEX and DAWN 8+ instruments, respectively (Wyatt Technology). Data were analyzed with ASTRA 6 software[38] and plotted with GraphPad.

In silico prediction of pathogenicity

Pathogenicity prediction was performed with AlphaMissense[39] and FoldX.[40] AlphaMissense scores and pathogenicity predictions were retrieved from https://github.com/google-deepmind/alphamissense. FoldX 5.0 was run locally using default settings, and the models of the crystallographic DHO (PDB 4C6C; 1.45 Å resolution) and ATC (PDB 5G1O; 2.1 Å resolution). Before performing calculations, the 'RepairPDB' command was used to fix the structures. Individual mutations were introduced using the 'BuildModel' command. Calculations were performed in 5 consecutive runs, and ΔΔG values were extracted from the FoldX output files. A value of 1.5 kcal·mol^{-1} was set as the stability change threshold, as previously suggested in other studies assessing the impact of missense mutations.[41,42]

Molecular dynamics

Molecular dynamic (MD) simulations were performed for the DHO dimer using GROMACS 2023 software.[43] The DHO WT (PDB ID 4C6I) and S1538L crystal structures were used as input for the solution builder module in CHARMM-GUI[44] (https://www.charmm-gui.org) and the CHARMM36m[45] force field was adopted. The system was prepared using the structures without ligands and the flexible loop in the closed conformation, and the non-standard carboxylated lysine residue (K1556) was parameterized with the CHARMM36 force field.[46] Zinc ions were not included in the system due to the complex parameterization of the catalytic center of the protein. The system pH was set to 7, and TIP3 water was added to the simulation in a rectangular box. Potassium and chloride counter-ions in a 0.15 M concentration were added to neutralize the solvated system. The Particle Mesh Ewald (PME)[47] was used to treat long-range electrostatic interactions, while a 12 Å cutoff scheme was used for van der Waals interactions. Simulations were performed at 310.15 K and 1 bar in an NPT ensemble. Two replicates of 500 ns were run for the WT and mutant dimers, and the trajectories were analyzed individually for each subunit using GROMACS analysis tools. Principal components analysis (PCA) was performed on the backbone atoms to reduce dimensionality and explore protein flexibility along the trajectory. The analysis was performed on single trajectories that concatenated the simulations of the dimer subunits in the two replicas fitted to the reference structure. The covariance matrix and PCA projection for the two first eigenvectors were computed with GROMACS analysis tools. Matplotlib[48] was used for PCA plot representation, Pymol (https://pymol.org/) and ChimeraX[49] for visual structural analysis, and GraphPad for other graphical representations.

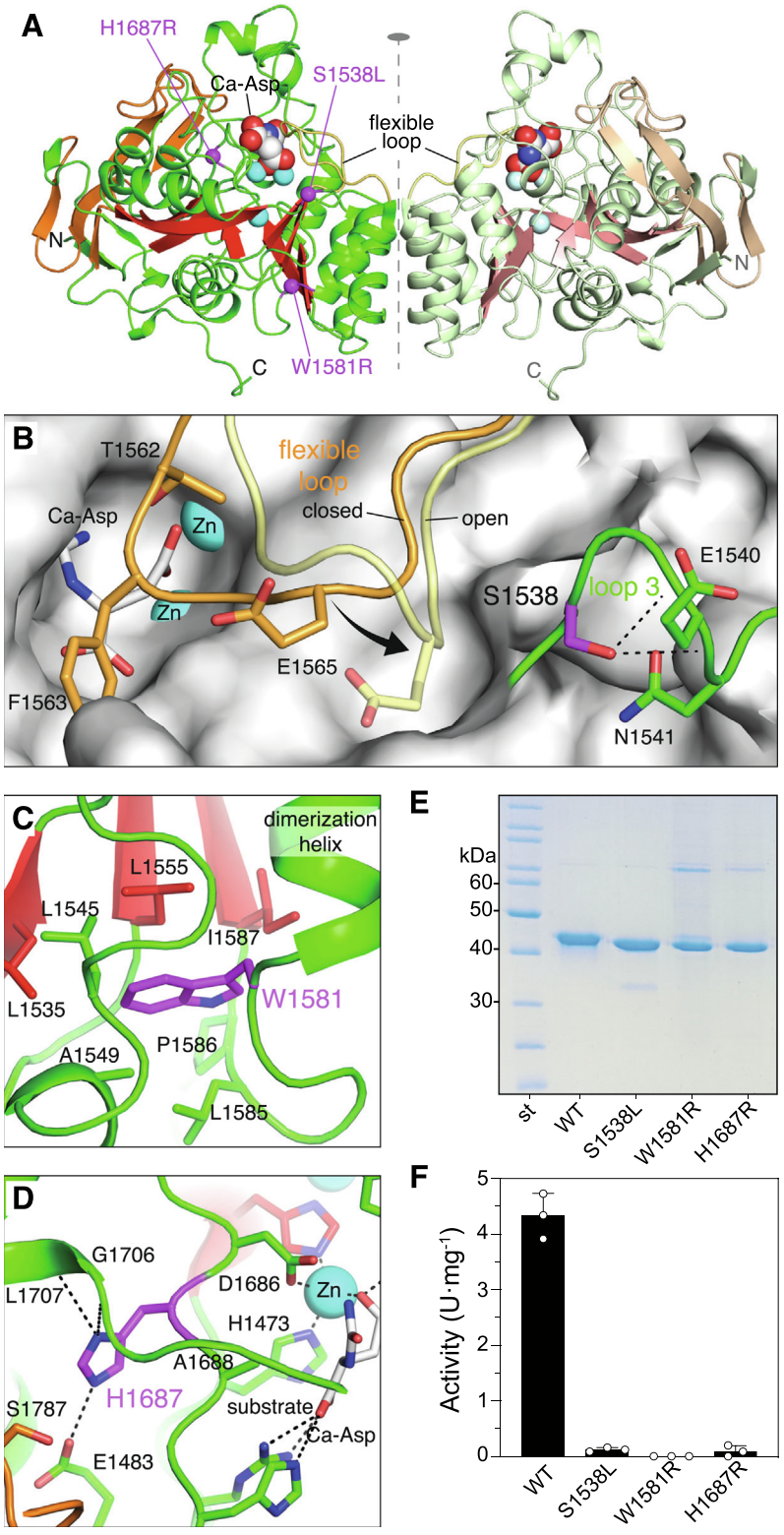

Figure 2. Pathogenic variants in CAD's DHO domain. A. Cartoon representation of the DHO dimer, with substrate Ca-Asp and Zn^{2+} cations depicted as spheres. The positions of pathogenic variants are indicated with magenta spheres. **B.** Surface representation of the DHO active site with bound Ca-Asp and the flexible loop in closed (orange) and open (yellow) conformations. Loop-3 is shown in green, with the side chain of S1538 in magenta. Dashed lines indicate electrostatic interactions. **C, D.** Detail views of the mutated residues (in magenta) and surrounding elements. **E.** SDS-PAGE of purified recombinant DHO mutants. **F.** Enzymatic activity of WT and DHO mutants shown in a scattered plot with three independent measurements. Error bars indicate standard deviation. Activity units (U) are nmol of dihydroorotate per min.

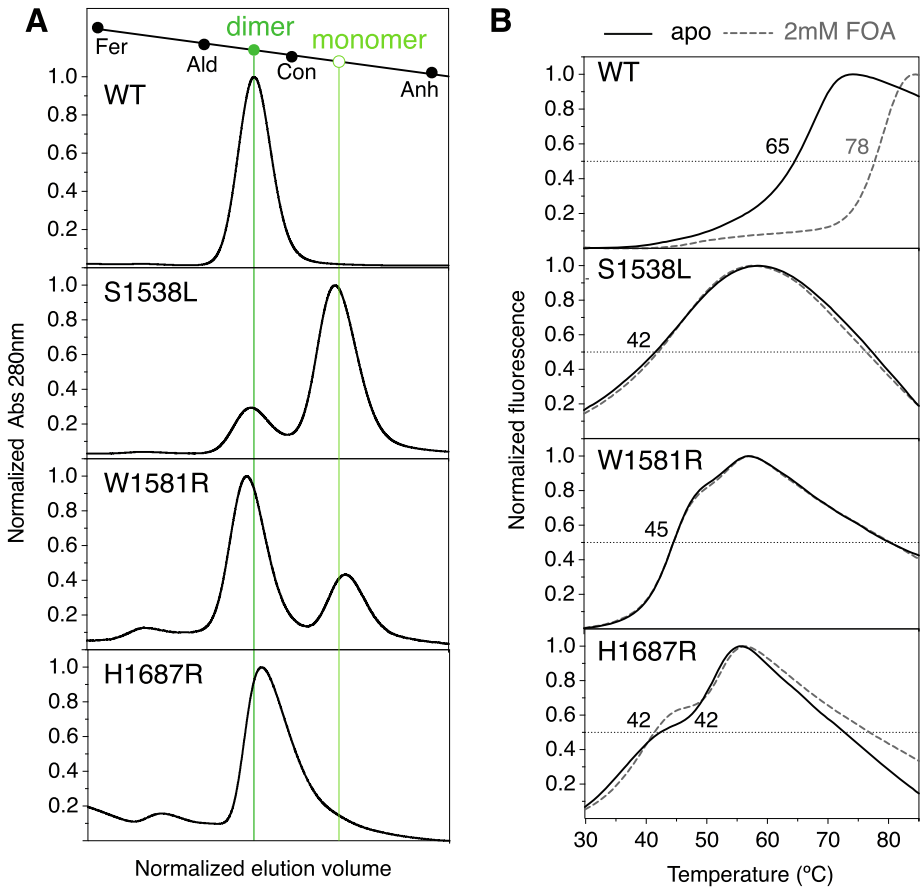

Figure 3. Oligomerization and stability of DHO mutants. **A.** SEC analysis of purified DHO proteins. Column calibration with proteins of known molecular weight: ferritin (440 kDa), aldolase (158 kDa), conalbumin (75 kDa), and carbonic anhydrase (29 kDa). **B.** Denaturing curves in the absence (apo) and presence of fluoroorotate (FOA) measured by scanning fluorimetry. Midpoint temperatures (T_m) are indicated.

Results

Characterization of pathogenic variants in CAD's ATC domain

The cell proliferation assay identified two pathogenic changes, R1986Q and P2186S, within CAD's ATC domain (Figure 1A).[24] This domain self-assembles into a homotrimer with one active site per subunit (Figure 1B).[20] Each active site contains binding sites for the substrates carbamoyl phosphate (CP) and aspartate and is complemented with a CP-loop from the adjacent subunit that positions CP for nucleophilic attack and stabilizes the transition state. Mutation P2186S affects an invariant residue within the active site that introduces a kink in the polypeptide chain and contacts the side chains of three also invariant residues –S2000, K2003 and E2005– in the CP-loop of the adjacent subunit (Figure 1C and Supplementary Figure 1). A substituting Ser at this position was predicted to distort the active site and hinder the approach of the CP-loop. On the other hand, residue R1986, located ~20 Å away from the active site and on the opposite face of the trimer, forms an intersubunit salt bridge with D2019 (Figure 1D). Both residues are highly conserved (Supplementary Figure 1); thus, mutation R1986Q was anticipated to disrupt the conserved interaction and destabilize the trimer.

To characterize the molecular alterations of these variants, we produced the ATC domain bearing the point mutations R1986Q and P2186S. The recombinant proteins were produced at a similar yield and purity as the wild-type (WT) protein, suggesting that the mutations did not have a noticeable effect on protein folding and stability. Size exclusion chromatography (SEC) analysis showed that ATC-P2186S eluted at the expected position for a homotrimer (molecular weight 105 kDa), whereas ATC-R1986Q behaved as a monomer (35 KDa) (Figure 1E). Using SEC coupled with multiangle light scattering (MALS) analysis, we observed that adding PALA (phosphonacetyl-L-aspartate), an inhibitor that mimics the transition state of the reaction,[50]

Table 1 Data collection and refinement statistics. Values for the highest resolution shell are shown in parentheses.

	S1538L+Ca-Asp	S1538A+Ca-Asp	S1538A apo
PDB deposition ID	9FS1	9FS2	9FS3
Data collection			
Wavelength	0.87313	0.97926	0.97926
Resolution range (Å)	73.08–1.21 (1.26–1.21)	47.22–1.12 (1.16–1.12)	44.43–1.18 (1.22–1.18)
Space group	$C222_1$	$C222_1$	$C222_1$
Unit cell parameters			
a, b, c (Å)	82.3, 158.7, 61.9	82.1, 158.6, 61.9	82.1, 158.5, 61.8
α, β, γ (°)	90, 90, 90	90, 90, 90	90, 90, 90
Total reflections	781,132 (24,483)	303,746 (27,639)	671,722 (63,734)
Unique reflections	119,378 (5,546)	153,846 (13,868)	130,558 (12,435)
Multiplicity	6.4 (6.7)	6.5 (6.1)	5.1 (5.0)
Completeness (%)	99.2 (91.5)	98.8 (91.1)	98.2 (95.0)
Mean I/sigma(I)	20.4 (0.8)	7.5 (0.8)	8.0 (0.9)
Wilson B-factor	13.1	11.0	11.7
R-pim	0.049 (1.048)	0.051 (0.963)	0.044 (0.762)
$CC_{1/2}$	0.992 (0.882)	0.998 (0.410)	0.998 (0.433)
Refinement			
Reflections used	119,320 (9,691)	152,046 (13,864)	129,893 (12,431)
R-factor/R-free	0.12/0.15	0.14/0.17	0.15/0.17
Number of atoms	3,284	3,526	3,360
Macromolecules	2,837	2,962	2,881
Ligands	32	93	63
Solvent	425	504	441
Protein residues	362	362	362
RMS (bonds) (Å)	0.011	0.014	0.009
RMS (angles) (°)	1.24	1.32	1.15
Ramachandran favored (%)	95.8	95.5	95.8
Ramachandran allowed (%)	3.6	3.7	3.4
Ramachandran outliers (%)	0.6	0.8	0.8
Rotamer outliers (%)	0.7	0.9	0.0
Average B-factor	19.21	16.65	16.48
Macromolecules	17.12	14.34	14.62
Ligands	14.85	23.92	25.08
Solvent	33.42	29.35	27.92

prompted the re-assembly of ATC-R1986Q into trimers. This result suggested that the multiple electrostatic interactions with PALA glued the CP-loop and active site elements from adjacent subunits and compensated for the missing salt bridge (Figure 1C, F).

Since active sites form at subunit interfaces, ATC must trimerize to be active. Thus, the oligomerization defect of ATC-R1986Q explains its near-zero enzymatic activity (Figure 1G). Notably, its residual activity was even lower than ATC-P2186S, which directly impairs substrate binding and catalysis by altering an invariant residue at the active site.

Characterization of pathogenic variants in CAD's DHO domain

The cell proliferation assay identified three pathogenic mutations that affected conserved residues in the DHO domain: S1538L, W1581R, and H1687R (Figure 1A and Supplementary Figure 2).[25] This domain forms a homodimer, with each subunit folding in an $(\alpha/\beta)_8$-barrel with an adjacent β-stranded region opposite the dimerization interface and a long C-terminal extension (Figure 2A).[18,23] The active site, formed by the loops connecting the carboxy end of the β-barrel with the surrounding α-helices, contains three Zn^{2+} cations and a flexible loop that closes over the substrate carbamoyl aspartate (Ca-Asp) and opens for dihydroorotate product release (Figure 2A, B). A preliminary structural analysis suggested that S1538L would disrupt the formation of hydrogen bonds in the loop bearing the mutation (loop-3), which is adjacent to the catalytic flexible loop (Figure 2B). On the other hand, W1581R replaces the Trp at the C-end of a dimerization helix with a positively charged side chain that would be in an unfavorable hydrophobic environment and cause severe steric clashes (Figure 2C), whereas H1687R introduces a bulky side chain next to a Zn-coordinating Asp (D1686), likely causing steric clashes and distortion of the active site (Figure 2D). The pathogenicity of the variants was correctly predicted by FoldX, with scores being two-fold higher

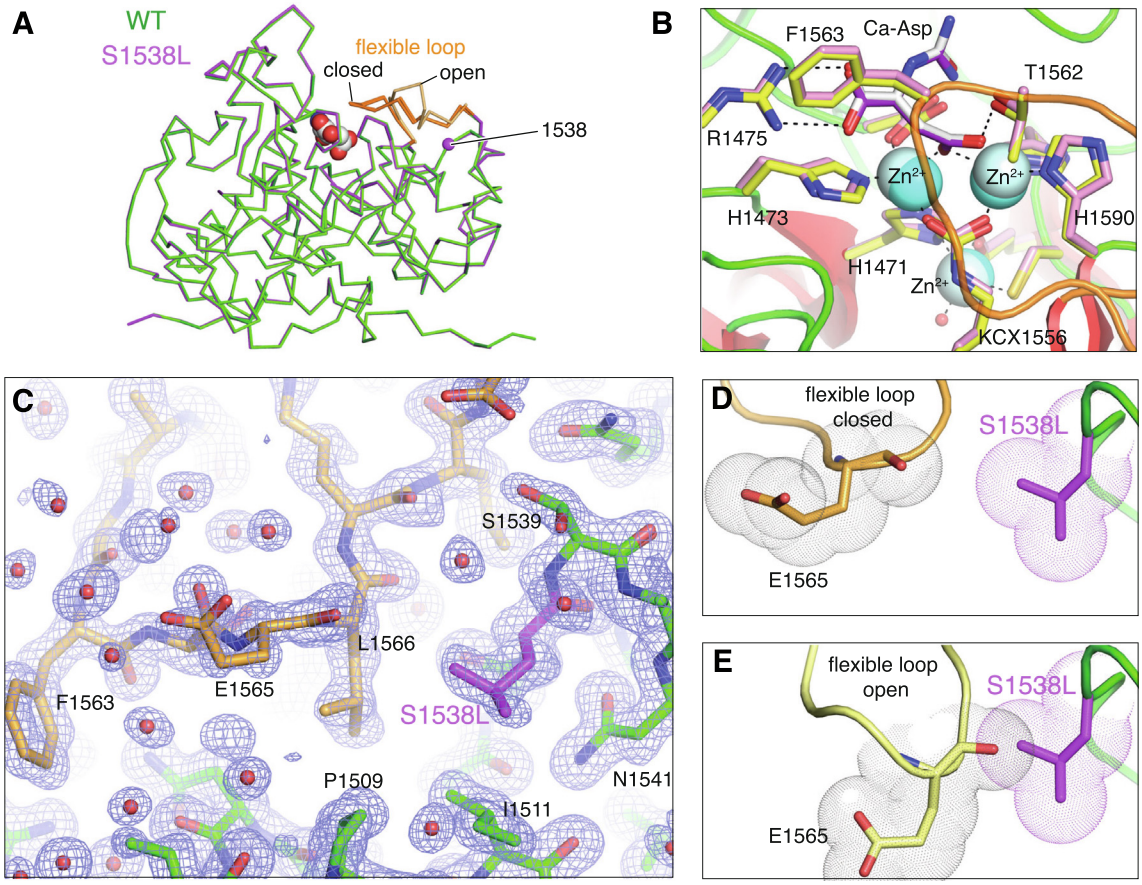

Figure 4. Structure of DHO S1538L mutant. A. Ribbon superposition of DHO WT and S1538L subunits. **B.** Superposition of the DHO WT (side chain carbon atoms in yellow) and mutant S1538L (pink) active sites. Dashed lines represent electrostatic interactions. **C.** Detail of mutant S1538L crystal structure with the flexible loop depicted in orange and the mutated Leu in magenta. The $2F_{obs}$-F_{calc} electron density map is shown as a blue mesh contoured at 1.0 σ. **D.** Close contact between the mutated Leu and residue E1565 in the flexible loop. Atom radii are represented as dot clouds. **E.** Model of the clash between the mutated Leu and the flexible loop in the open conformation.

for W1581R and H1687R compared to S1538L, whereas AlphaMissense considered S1538L as benign (Supplementary Table 1).

To characterize the molecular alterations of these variants, we produced isolated DHO domains with the point mutations (Figure 2E). DHO-S1538L was expressed and purified at yields comparable to DHO-WT. In contrast, mutants DHO-W1581R and DHO-H1687R consistently showed ∼20-fold lower yields despite repeated attempts, indicating that these mutations negatively impact protein production.

All three mutated DHO domains showed impaired enzymatic activity (Figure 2F). The residual activity of DHO-S1538L (v = 0.1 U·mg^{-1}) was ∼40-fold lower than DHO-WT (v = 4.2 U·mg^{-1}), whereas DHO-W1581R and DHO-H1687R exhibited no activity despite testing protein concentrations 10-fold higher.

Analysis of the oligomeric state by SEC showed that similar to DHO-WT, DHO-H1687R eluted as a single peak at the position expected for a homodimer (Figure 3A). In turn, DHO-S1538L and DHO-W1581R eluted in two peaks, corresponding to a different proportion of dimers and monomers. Mutant DHO-W1581R behaved mostly as a dimer with a 30% monomer fraction, whereas DHO-S1538L was mostly dissociated (80%) (Figure 3A).

We compared the stability of the proteins by differential scanning fluorimetry (DSF) in the absence and presence of fluoroorotic acid (FOA), a competitive inhibitor that mimics the binding of dihydroorotate to the active site.[18] The DHO-WT denaturation curves showed a midpoint temperature (Tm) of 65 °C and an increment of 13 °C upon binding to FOA (Figure 3B). In turn, the mutants had compromised stability, with Tm's falling within the range of 42–45 °C and no increase in stability in the presence of FOA.

In summary, these results indicated that reduced stability, compromised substrate binding and impaired enzymatic activity may contribute to the pathogenicity of the mutations in the DHO domain. Notably, two mutations, S1538L and W1581R,

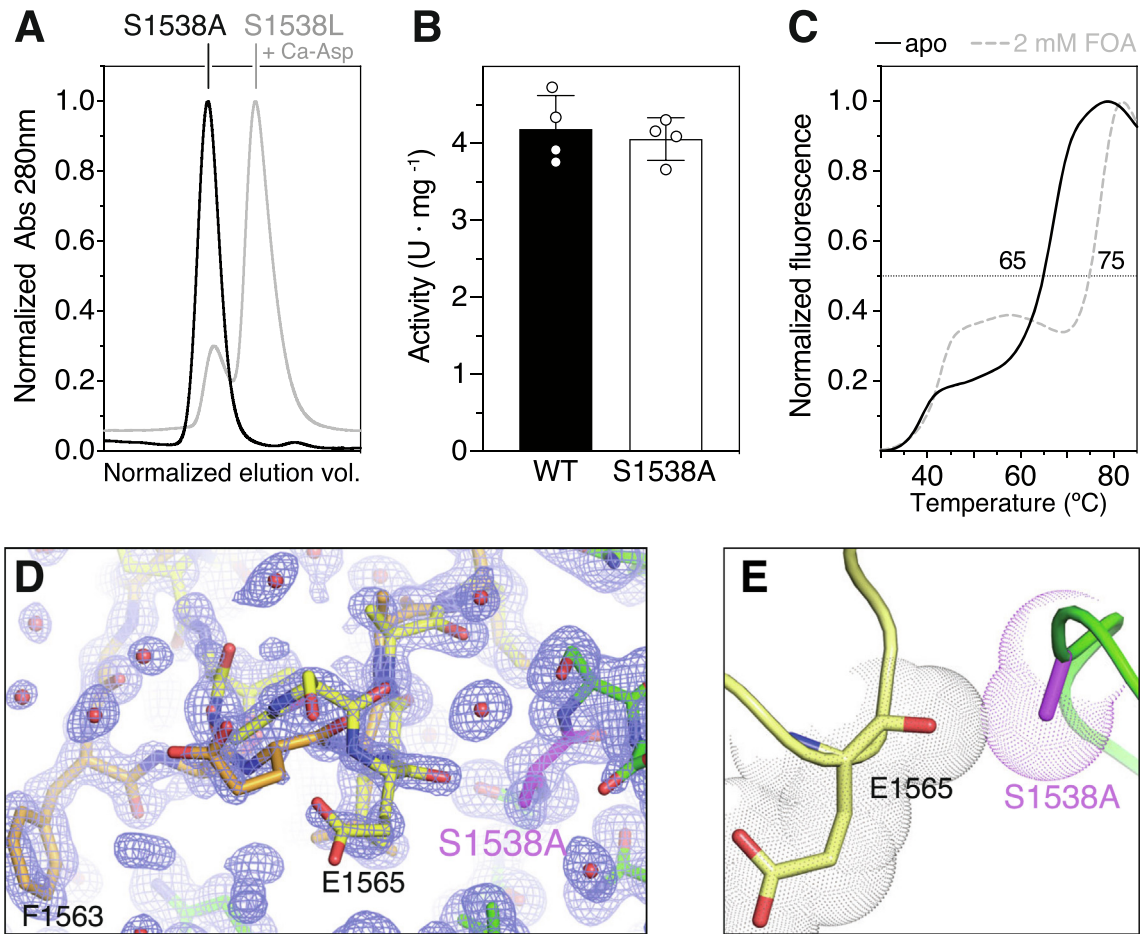

Figure 5. Characterization of DHO S1538A mutant. A. SEC analysis of purified mutant S1538A (black trace) shows the formation of dimers. In the presence of 2 mM Ca-Asp, the mutant S1538L (gray trace) continues as a monomer. **B.** Activity assay of mutant S1538A. **C.** Thermal stability assay of mutant S1538A in the absence and presence of 2 mM FOA. **D.** Detail of mutant S1538A crystal structure. The $2F_{obs}$-F_{calc} electron density map, shown as a blue mesh contoured at 1.0 σ, indicates a mixed population of molecules with the flexible loop in closed (orange) and open (yellow) conformations. **E.** Close contact between the substituting Ala and the flexible loop, with atom radii represented as dot clouds.

also promoted the dissociation of the DHO dimer, suggesting that this was a novel factor to consider when evaluating the pathogenicity of CAD clinical variants.

S1538L hinders the movement of the DHO catalytic flexible loop

To better understand the impact of the pathogenic mutations in the DHO domain, we sought to determine their crystal structures. Mutants DHO-W1581R and DHO-H1687R could not be concentrated without significant protein losses and did not crystallize in the conditions reported for DHO-WT or after extensive screenings, supporting the destabilizing effects of these mutations. However, DHO-S1538L crystallized using the established conditions for DHO-WT, and the structure was determined at 1.5 Å resolution (Table 1).

DHO-S1538L only crystallized in the presence of the substrate Ca-Asp. Although predominantly monomeric in solution, the structure revealed a homodimer with subunits indistinguishable from DHO-WT (Figure 4A), suggesting that the higher protein concentration and favorable packing in the crystal lattice enhanced the formation of the dimer. The high-resolution electron density maps showed the Zn^{2+} cations and residues in the active site in virtually identical positions as DHO-WT and a molecule of Ca-Asp interacting with the flexible loop in the closed conformation (Figure 4B). The substituting Leu exhibited well-defined electron density and, in principle, did not show any alterations that could explain the impaired enzymatic activity (Figure 4C). However, the Leu side chain would clash against E1565 if the catalytic flexible loop adopted the open conformation (Figure 4D, E). This observation explained that the protein only crystallized in the

closed state favored by the binding of Ca-Asp. We hypothesized that in the absence of Ca-Asp, the flexible loop could move away from the active site to a position different from the canonical open conformation that destabilized the subunit and affected dimerization.

We also tested whether incubating mutant S1538L with 2 mM Ca-Asp and adding the substrate in the SEC column buffer favored the formation of the dimer, but the protein eluted at the expected position for a monomer (Figure 5A). This suggested that the higher protein concentration used for crystallization and the growth of the crystal itself, which depends on the packing of a dimer in the crystal lattice, favor interdomain interactions that are otherwise too weak to maintain the S1538L dimer in solution.

To demonstrate that the inactivation of the enzyme is due to a steric clash between the mutated Leu and the loop in the open conformation, we substituted S1538 with Ala. The isolated DHO domain bearing mutation S1538A behaved as a homodimer in solution and exhibited similar enzymatic activity as the WT and comparable thermal stability (Figure 5A–C). The structures of DHO-S1538A, free and in the presence of Ca-Asp, were determined at 1.2 Å resolution (Table 1). As for DHO-WT, the structures showed the flexible loop in alternate open and closed conformations (Figure 5D), and in agreement with the reversibility of the reaction, the crystal grown with Ca-Asp showed an average electron density corresponding to a mixture of substrate and product in the active site (Supplementary Figure 3). These results proved that disrupting the electrostatic interactions of the S1538 side chain within loop-3 had a minor impact on the stability and activity of the protein and that its substitution with alanine but not with leucine is compatible with the canonical open conformation of the flexible loop (Figures 4E and 5E).

Next, we compared the movement of the flexible loop in DHO-WT and DHO-S1538L using molecular dynamics (MD). Simulations for the protein dimers started with the flexible loop in the closed conformation and no substrate in the active site. Over the 500 ns trajectories, DHO-S1538L exhibited overall increased flexibility compared to DHO-WT, particularly in the flexible loop, the loop-3 bearing the point mutation, and the dimerization helices (Figure 6A). Whereas in DHO-WT, the flexible loop fluctuated between the known open and closed conformations, in DHO-S1538L, the loop moved from the closed state to distant positions that were different from the canonical open conformation. This was monitored by measuring the distance between the Cα atom of F1563 at the tip of the flexible loop relative to its position in the initially closed conformation (Figure 6B). The increased flexibility of the mutant was also apparent by comparing the positions of the Cα atoms of residues F1563 and G1543, the residue at the tip of loop-3, along the trajectories (Figure 6C). Principal components analysis (PCA) of the trajectories showed major conformations changes along the first eigenvector (principal component-1; PC1), corresponding to the movements of the flexible loop, loop-3 and adjacent dimerization helices (Figure 6D). The larger variations along PC1 and PC2 indicated that mutation S1538L favored new structural states or increased the flexibility of the existing ones compared to DHO-WT.

The simulated time allowed us to observe local movements of the flexible loop and other protein elements but was insufficient to capture their impact on larger collective motions, such as dimer dissociation, which likely requires microsecond-scale simulations.[51] Overall, these findings supported that mutation S1538L inactivates the enzyme by altering the movement of the catalytic flexible loop and also increases the flexibility in this loop, in loop-3 bearing the mutation, and in the adjacent helices, which may impair DHO dimerization. However, the impact of impaired dimerization on the activity of the full-length protein remained unclear.

DHO dimerization is required for CAD activity

The effect of mutation S1538L was twofold, as it impacted the movement of the flexible loop and

Figure 6. DHO molecular dynamics simulations. A. Backbone root mean square fluctuation (RMSF) for DHO WT and mutant S1538L, showing increased flexibility in the mutant, mainly in loop-3 bearing the mutation, flexible loop and first dimerization helix (α4). Lines are mean values, and shaded areas represent the standard deviation of two independent simulations of the dimers. **B.** Variation of the distance in the position of the Cα atom or residue F1563, at the tip of the flexible loop, relative to its initial closed conformation along the 500 ns trajectories. **C.** Perpendicular views of the DHO model, with spheres indicating the dispersion in the positions of the Cα atoms of residues G1543 and F1563 in the WT (cyan) and mutant S1538L (magenta) during simulations. **D.** Principal component analysis (PCA) of the protein models along the MD trajectories (represented as dots). Higher populated conformational states are indicated with a color gradient, with yellow being the most populated. The most populated conformations of the WT (depicted in cyan) and mutant S1538L (magenta) proteins are shown in ribbon representation and superposed with the initial closed state in the trajectory (in green).

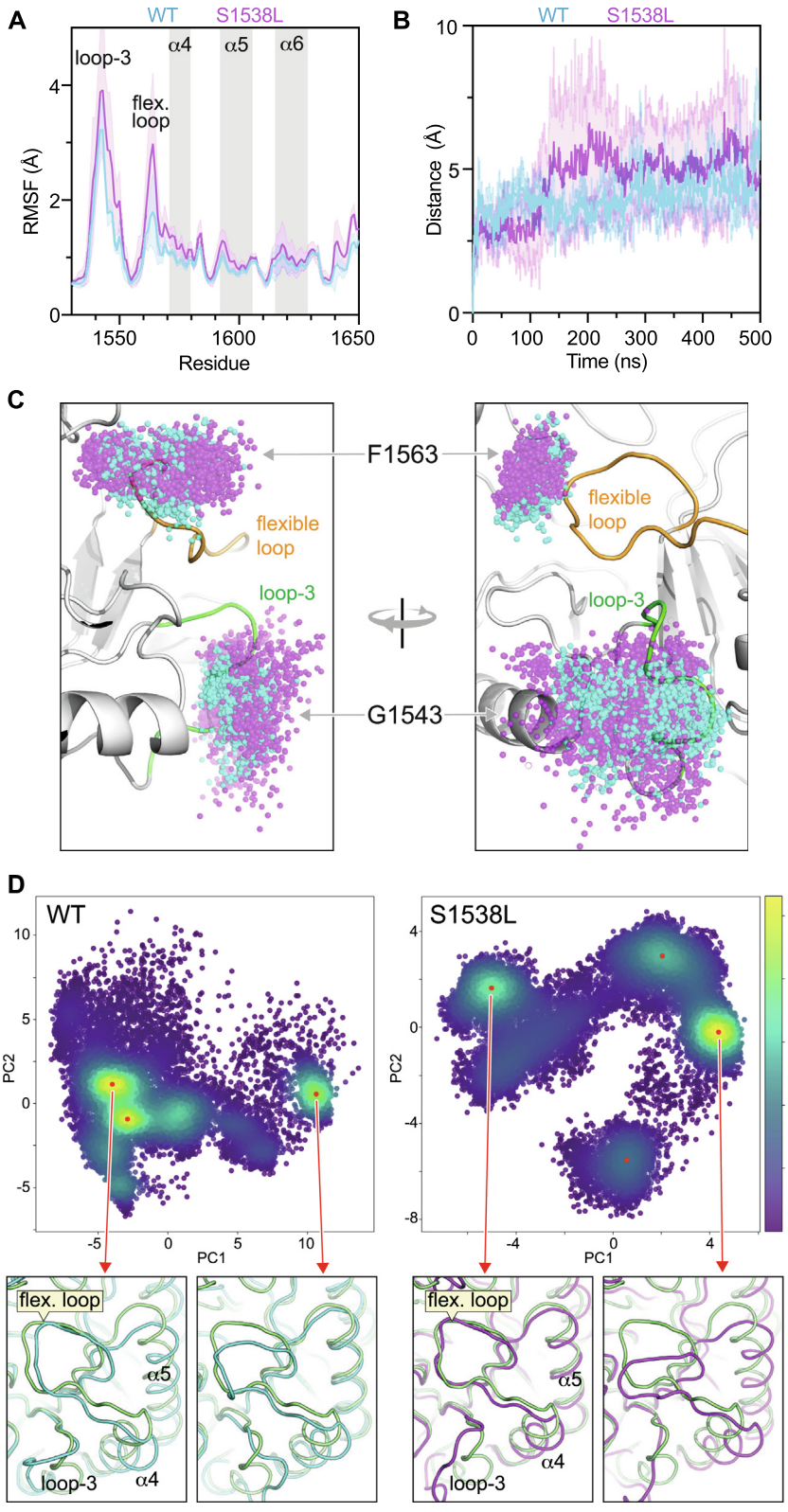
A
WT
S1538L
loop-3
α4
α5
α6
flex. loop
RMSF (Å)
Residue
B
WT
S1538L
Distance (Å)
Time (ns)
C
F1563
flexible loop
loop-3
G1543
D
WT
S1538L
PC1
PC2
flex. loop
α5
α4
loop-3

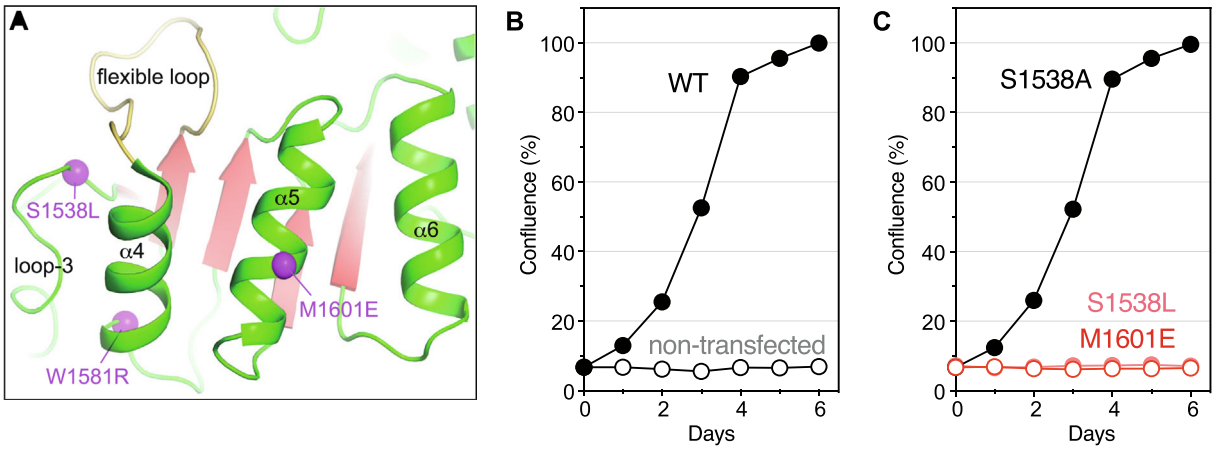

Figure 7. CAD is inactivated by impaired DHO oligomerization. A. Cartoon representation of the DHO dimerization interface viewed from the other subunit in the dimer. The Cα atoms of the mutated residues are shown as magenta spheres. M1601E is located in the middle of the central dimerization helix and impedes the oligomerization by charge repulsion and steric clashes with the same residue in the other subunit. **B,C.** Growth complementation assay of CAD-knockout cells grown without uridine and transfected with GFP-CAD WT (**B**) or bearing point mutations (**C**). Each point represents the mean and standard deviation of two independent experiments, counted in duplicates.

dimerization. To investigate to what extent a defect in DHO dimerization contributed to pathogenicity, we turned to another mutation, M1601E, which we previously designed to identify the DHO dimerization interface (Figure 7A).[18] Our prior study showed that DHO-M1601E behaved as a monomer in solution and had similar thermal stability as DHO-WT. Interestingly, DHO-M1601E retained 50% of the WT activity,[18] suggesting that dimerization could somehow affect the movement of the catalytic flexible loop but was not essential for the DHO enzymatic activity. However, the impact of mutation M1601E within the full-length CAD protein had not been tested.

We introduced mutation M1601E in the full-length CAD construct and assessed its functionality in the cell proliferation assay. Transfection of CAD-M1601E failed to rescue the growth of CAD-KO cells under uridine-free conditions, as seen for the pathogenic variants, including S1538L (Figure 7B, C). This result indicated that mutation M1601E impairs CAD activity and, thus, the *de novo* synthesis of pyrimidine nucleotides. In turn, CAD-S1538A effectively recovered the growth phenotype, confirming the neutral effect of this mutation in both the isolated DHO domain and the full-length protein (Figure 7C).

In summary, our finding with mutation M1601E indicated that DHO dimerization is essential for CAD function. Therefore, we also concluded that the dimerization defect contributes to the pathogenicity of the S1538L variant.

Predicted structure of CAD hexamers

The low stability of full-length human CAD protein has thus far impeded its structural characterization through various methods, including cryo-electron microscopy. Thus, we turned to the AlphaFold (AF) artificial intelligence prediction program to advance our understanding of the protein's architecture.[52] The available CAD model in the AF database (https://alphafold.ebi.ac.uk/entry/P27708) correctly predicts the structures of the ATC and DHO domains and generates a reliable GLN/CPS-2 heterodimer, closely resembling *E. coli* CPS and human CPS-1 structures (Supplementary Figure 4A).[53,54] The high value for the pLDDT confidence measure (>90) indicated high accuracy in the modeled domains but not for the linkers (pLDDT < 50), particularly for the 96 aa connecting DHO and ATC. Thus, the model fails to provide a reliable orientation of the ATC domain, as indicated by the predicted aligned error (PAE) calculations, which we attributed to the low structural complexity of the long linker to the rest of the protein (Supplementary Figure 4A).

Nonetheless, the models obtained by running AF-2 locally or using the AF-3 webserver consistently predicted the interaction between ATC and the L2 and L3 domains of CPS-2 (Figure 8A and Supplementary Figure 4B, C). The scores for the template modeling (pTM > 0.83) and the interface predicted template modeling (ipTM = 0.76) indicated a low error in the overall predicted fold and in the relative positioning of the domains. The result was consistent whether using the full-length protein or the isolated enzymatic domains as input. In this model, the orientation of the ATC domain was compatible with its oligomerization as a homotrimer observed by X-ray crystallography (Figure 1C). By superimposing three copies of the predicted CAD subunits with the crystal structure of the ATC trimer, we constructed a model of a

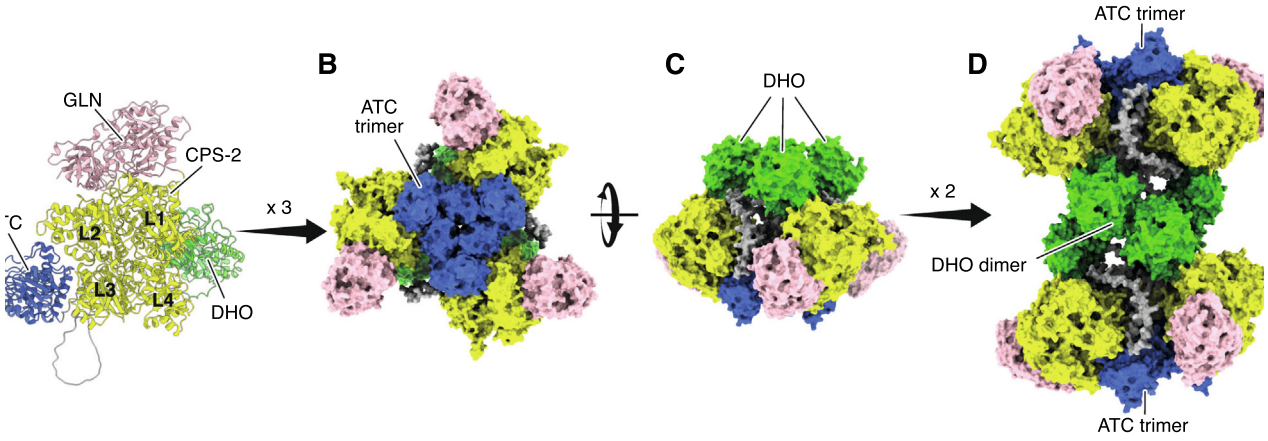

Figure 8. Model of CAD hexamer. A. Cartoon representation of the model generated by AlphaFold for the CAD subunit, with each enzymatic domain depicted in a different color. **B, C.** Perpendicular views of the CAD trimer obtained by superimposing three copies of the AlphaFold model on the crystal structure of the ATC trimer. **D.** Model of the CAD hexamer generated by the superposition of two CAD trimers on the crystal structure of the DHO dimers.

CAD trimer that showed no steric clashes among domains (Figure 8B, C). We obtained a similar model among the top five solutions of AF-2 upon modeling a CAD trimer. Within this trimer, the three DHO domains were oriented on the same side of the particle (Figure 8C), which was compatible with the formation of the DHO homodimers observed in the crystal structure (Figure 2A). Based on the symmetry of the DHO dimers, we positioned a second CAD trimer, obtaining a hexameric particle (a dimer of trimers) (Figure 8D and Supplementary movie). The resulting model, obtained simply by applying the known symmetries of the ATC and DHO domains to the AF subunit solution, shows no clashes, and only small adjustments in two DHO subunits would be needed to match exactly the interactions observed in the crystal structure. We find it highly improbable that a hexameric particle could form without significant steric clashes if the CAD domains were oriented differently, which is an indication to us that the model is likely correct.

Discussion

The assembly of CAD into a hexameric particle has remained unresolved, but likely supports concatenated enzymatic reactions, subunit cooperativity,[20] metabolite channeling,[28,55,56] allosteric control,[3] modulation by phosphorylation,[57–60] and may also enable the formation of a "pyrimidinosome" with other proteins in the nucleotide biosynthetic pathway.[61] While so far, the variants in CAD-deficient patients have been shown to affect protein stability or active site elements,[25] this study shows that mutations disrupting oligomerization are pathogenic and that the assembly of CAD into a mega-enzyme is essential for nucleotide synthesis.

The importance of ATC oligomerization for CAD assembly was first shown *in vitro* by D. Davidson's group.[62,63] Based on the *E. coli* ATC structure and sequence conservation, they proved that disrupting the ion pair D2009–R2187 in ATC caused hamster CAD to dissociate into monomers, severely reducing activity, and that PALA or CP binding restored oligomerization. Here, we demonstrated a similar defect as the pathogenic mechanism of variant R1986Q, found in homozygosis in a patient and one deceased sibling.[24] This mutation disrupts the R1986-D2019 ion pair, leading to ATC trimer dissociation and a residual activity that is likely due to partial reassembly upon CP binding (Figure 1E, G). PALA also compensates for the loss of the ion pair and restores oligomerization (Figure 1F), indicating that R1986Q does not cause protein misfolding. Notably, this oligomerization defect is as harmful as directly mutating an invariant residue at the active site (Figure 1G). In the context of the full-length protein, we previously showed that CAD-R1986Q fails to rescue the growth of CAD-KO cells without uridine,[24] thus confirming that the defect in ATC oligomerization blocks pyrimidine nucleotide synthesis. Very likely, the variants D2019A and D2019N, found at low allele frequency in the population (10^{-6}–10^{-7},gnomAD v4.0), are also pathogenic since they impair this conserved ion pair but have not been found in CAD-deficient patients yet.[25]

The role of the DHO domain in CAD assembly was less understood. The discovery that the isolated human DHO domain forms a homodimer was insightful but not entirely unexpected,[18,19,64] given that bacterial homologs also form dimers, although using different interacting interfaces.[18] We found that the human DHO dimer was virtually identical to the pseudo-DHO domain in the CAD-like protein from fungi.[23] In these organisms, GLN,

CPS-2 and ATC are fused into a CAD-like polypeptide with an inactive pseudo-DHO domain, while an independent monofunctional protein carries out this enzymatic activity.[65] The structural similarity between human DHO and fungal pseudo-DHO homodimers suggested a key role in assembling CAD into a "dimer of trimers" (a hexamer).[23] Now, the characterization of pathogenic variants confirms that DHO dimerization is essential for CAD function.

Two DHO variants, H1687R and W1581R, were found in compound heterozygosity via post-mortem exome sequencing in one patient and in another unrelated patient from the same city who improved with uridine treatment[25] (Dr. P Sanchez-Pintos, personal communication). Both mutations affect the folding and stability of the DHO domain, with reduced production yields, decreased thermal stability, and no enzymatic activity (Figures 2E, F and 3B). Additionally, W1581R caused partial dissociation (Figure 3A) due to its position at one dimerization helix (Figures 2C and 7A). Another DHO variant, S1538L, was found alongside a splicing variant in a 1-year-old patient who also improved with uridine[25] (Dr. J Kenny, personal communication). S1538L, though less destabilizing than the previous mutations, inactivated the enzyme and promoted dimer dissociation (Figures 2F and 3A). The structure and MD simulations indicate that the mutation of S1538 to Leu, but not to Ala, alters the correct movement of the catalytic flexible loop (Figures 4C–E and 5D, E). This flexible loop acts as a lid over the active site in both *E. coli* and human DHOs, playing a crucial role in the reaction cycle: it closes to bind and orient Ca-Asp, increases its electrophilicity, excludes water, stabilizes the transition state, and then opens to release dihydroorotate.[27,66,67] Only two distinct open and closed conformation states have been observed in various human DHO structures.[27] S1538L prevents the canonical open conformation, forcing the catalytic loop into more distant and flexible conformations (Figure 6), and also increases the flexibility of loop-3 and adjacent dimerization helices, explaining the dimerization issues. Notably, we previously observed that replacing the flexible loop of human DHO with that of *E. coli* resulted in an inactive chimeric protein with impaired dimerization.[27] Altogether, these results suggest that changes in the flexible loop's movement can affect dimerization and vice versa.

The dual impact of S1538L on enzymatic activity and dimerization left unclear whether impaired DHO oligomerization contributes to its pathogenicity. To explore this, we examined the non-clinical mutation M1601E, designed to confirm the role of helices α4, α5 and α6 in DHO dimerization (Figures 2A and 7A).[18] M1601 is centrally located in helix α5, and the large, negatively charged Glu side chain would clash with the same residue in the adjacent subunit, hindering dimerization. Previously, we found that monomeric DHO-M1601E showed similar stability to DHO-WT but had 50% reduced activity,[18] which we now attribute to increased flexibility in the dimerization helices and indirect alterations in the flexible loop. Now, using the CAD-KO proliferation assay, we demonstrated that M1601E impairs full-length CAD function (Figure 7B, C). Given that CPS-2 is the rate-limiting step in CAD overall reaction (~30-fold slower than DHO),[3,62] the 50% reduction in DHO activity alone does not explain the effect of this mutation. Instead, our data indicate that the pathogenicity of M1601E arises from impaired CAD oligomerization. Thus, we conclude that DHO dimerization is essential for CAD assembly and that mutations altering the DHO intersubunit interface will be pathogenic.

CAD is a challenging protein, and despite many efforts, including our own, X-ray crystallography and cryo-EM have not succeeded in resolving its structure. To our surprise, and in a mixture of joy and dejection at the superiority of artificial intelligence, AlphaFold helped generate a CAD model that likely reflects the true architecture. Although it requires experimental verification, the model helps explain the pathogenicity of the studied variants (Table 2). It reveals two layers of ATC trimers surrounded by GLN/CPS-2 heterodimers connected by three central DHO dimers (Figure 8). The GLN domains protrude, while CPS-2 interacts only with ATC and DHO within its subunit. The ATC and DHO active sites face outwards, contrary to our previous hypothesis of an internal reaction chamber.[23] The exit of the tunnel connecting the different active sites within CPS-2 is near the ATC active site for release of the unstable CP.[53,54] The gaps between the CPS-2 domains are partially filled by the linkers connecting DHO and ATC, and the phosphorylation of S1859 in this linker is proposed to favor CAD oligomerization.[59] The model underscores the importance of ATC and DHO oligomerization for forming the CAD hexamer. In particular, DHO plays (literally) a central role, explaining the accumulation of pathogenic mutations in this domain and the structural conservation of the inactive pseudo-DHO domain in fungal CAD-like proteins. Thanks to the finding and characterization of the pathogenic variants R1986Q and S1538L, and of mutation M1601E, we can conclude that CAD must assemble into this large complex for proper cellular function. However, beyond forming intersubunit ATC active sites, the purpose of this mega-enzyme remains unclear and may relate to its integration with other cellular components.

Given CAD's need to form a functional hexamer, we questioned whether variants with impaired oligomerization could disrupt normal protein function, acting as dominant negatives. For instance, the S1538L variant with impaired DHO dimerization could still oligomerize with WT protein via the ATC domain, "poisoning" functional CAD

Table 2 CAD pathogenic variants and predicted mechanism based on the structure.

Variant	Predicted impact	Refs.
GLN domain		
M33R	Met at interface with CPS-2; the larger and positively charged Arg side chain impairs interactions with CPS-2 and blocks the channeling of ammonia.	24,5,6
G58S	Gly in a sharp turn of a loop at the CPS-2 interface; Ser substitution causes steric clashes, disrupting interactions with CPS-2.	25
R238C	Arg side chain forms electrostatic interactions with solvent-exposed elements; Cys substitution disrupts these stabilizing interactions.	25
G296E	Gly at active site forms H-bond with substrate glutamine; Glu introduces steric clashes and charge repulsion, distorting the active site and blocking substrate binding.	24
N320S	Asn side chain forms H-bonds with elements near the active site; Ser disrupts H-bonds, impairing substrate binding.	24
CPS-2 domain		
P454R	Pro side chain makes hydrophobic and Van der Waals contacts with adjacent elements; Arg's larger and positively charged side chain is in unfavorable environment and causes steric clashes.	13
G526R	Gly favors a sharp turn not permitted for other residue types, including Arg.	24
R742Q	Arg side chain at the active site; Gln substitution disrupts phosphorylation of carbamate.	24
P796T	Unclear effect. Pro in solvent-exposed loop likely tolerates Thr substitution.	24
V999M	Val side chain involved in hydrophobic cluster; Met's larger and more polar side chain causes steric clashes in unfavorable environment.	6,14
R1033Q	Arg forms a salt bridge with E1009 in an adjacent loop at the ATC interface; Gln substitution disrupts this stabilizing interaction and alters ATC contacts.	24
P1171Q	Pro in cys conformation in a sharp turn; Gln substitution causes steric clashes in a cluster of hydrophobic residues.	24
G1290S	Gly at contact point between secondary elements; Ser substitution introduces steric clashes.	13,24
DHO domain		
R1475Q	Arg side chain binds substrate carboxylate group at the active site; Gln hampers substrate binding	25
K1482M	Lys side chain orients catalytic residues R1475 and H1690 in active site; Met substitution hampers correct formation of active site.	25
S1538L	Ser next to catalytic flexible loop; Leu substitution hinders normal movement of the catalytic loop and indirectly disrupts DHO dimerization.	25, this paper
K1556T	Carboxylation of Lys side chain coordinates two Zn^{2+} ions at the active site; Thr substitution disrupts active site formation.	24
W1581R	Trp at C-end of dimerization helix; Arg substitution causes steric clashes and impairs hydrophobic interactions.	25, this paper
R1617Q	Arg side chain forms electrostatic interactions between adjacent structural elements; Gln substitution disrupts these stabilizing interactions	25
H1687R	Mutation introduces a bulky side chain next to Zn-coordinating D1686, causing steric clashes and distortion of the active site	25, this paper
R1722W	Arg forms electrostatic interactions between adjacent structural elements, including ion pair with E1671; Trp disrupts these stabilizing interactions	25
R1785C	Arg at interface with CPS-2; Cys substitution impairs interdomain contacts	24
R1785H	Arg at interface with CPS-2; His substitution impairs interdomain contacts	25
R1789Q	Arg side chain makes H-bonds and salt bridge with D1530; Gln substitution impedes these stabilizing interactions, and affects the positions of the C-terminal extension.	68
R1810Q	Arg anchors the DHO C-terminal extension to the globular domain through multiple H-bonds; Gln substitution impairs these stabilizing interactions and the anchoring of the C-terminal extension.	6
ATC domain		
E1954K	Glu makes intersubunit salt bridge; Lys substitution impairs oligomerization	6,20
R1986Q	Arg makes an intersubunit H-bonds and a salt bridge; Gln substitution favors the dissociation and inactivation of the ATC catalytic trimer.	24, this work
L1987V	Leu is part of a hydrophobic cluster; a substituting Val is in a favorable environment, but reduces contacts due to its smaller side chain.	24
R2024Q	Arg side chain binds the substrate at the active site; Gln substitution impedes correct formation of active site.	4,20
R2110L	Solvent-exposed Arg forms electrostatic interactions with nearby structural elements; a substituting Leu is in an unfavorable environment, and disrupts these stabilizing interactions.	24
E2128K	Glu in solvent-exposed positio, forms electrostatic interactions with adjacent Arg residues; Lys substitution disrupts these interactions and introduces charge repulsion.	24
P2186S	Pro introduces a sharp turn that shapes the active site, and interacts with K2003 from adjacent subunit; Ser substitution distorts the active site.	24

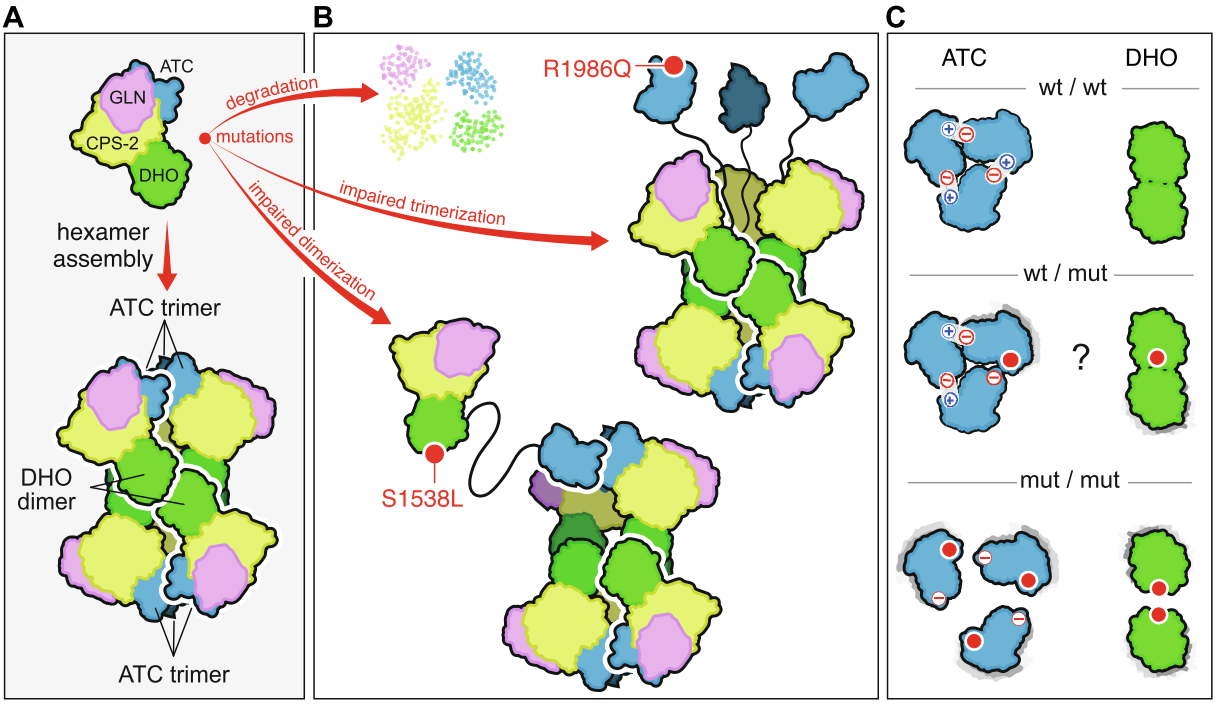

Figure 9. Assembly of CAD pathogenic variants. A. Proposed model for the assembly of CAD into a hexamer or a "dimer of trimers". **B.** Pathogenic mutations affecting oligomerization (red circles) could lead to protein degradation or "poison" the formation of functional particles. **C.** Three scenarios for the oligomerization of WT and mutated ATC and DHO domains. "+" and "−" signs indicate the ion pair between R1986 (+) and D2019 (−).

complexes (Figure 9A, B). Similarly, R1986Q with impaired ATC trimerization could oligomerize through the DHO domain. However, parents carrying an oligomerization-impaired CAD variant in one allele did not manifest the disease, indicating a recessive effect. This may be due to reduced stability and degradation of pathogenic variants or only subunits with intact DHO and ATC being incorporated into complexes. Another possibility is that mutations may weaken but not completely prevent oligomerization with WT (Figure 9C). In our in vitro assays, only mutant proteins are present, as in R1986Q homozygotes or S1538L haploinsufficient patients. However, in heterozygosity (as in the parents), pathogenic variants might still oligomerize with WT proteins, forming imperfect but partially functional complexes. For example, ATC-R1986Q might form heterotrimers with WT because the mutant retains residue D2019 to form an ion pair with R1986 in the WT (Figure 9C). Similarly, a DHO-S1538L could potentially dimerize with WT. For either of these scenarios or others we may not have considered, mutations S1538L and R1986Q are recessive. However, we do not discard that other oligomerization-defective variants could be dominant. For instance, M1601E likely prevents dimerization with WT without destabilizing the DHO domain,[18] suggesting it could have a dominant effect. Given the severity of the disease and its early manifestation, such dominant variants may appear *de novo* in heterozygosity with unaffected CAD variants, complicating diagnosis.

In summary, identifying and characterizing pathogenic variants has enriched our understanding of CAD, showing that oligomerization into a hexameric complex is essential for its function in nucleotide biosynthesis. Defects in this assembly must be carefully considered when assessing the pathogenicity of new variants. We look forward to experimentally confirming the predicted structure of this mega-enzyme to further clarify its mechanisms and related disease alterations.

CRediT authorship contribution statement

Francisco Del Caño-Ochoa: Writing – review & editing, Writing – original draft, Supervision, Investigation, Formal analysis. **Lobna Ramadane-Morchadi:** Writing – review & editing, Writing – original draft, Methodology, Investigation, Formal analysis, Conceptualization. **Lluís Eixerés:** Writing – review & editing, Visualization, Investigation, Formal analysis. **María Moreno-Morcillo:** Writing – review & editing, Investigation, Formal analysis. **Rafael Fernández-Leiro:** Writing – review & editing, Visualization, Validation, Investigation, Funding

acquisition, Formal analysis. **Santiago Ramón-Maiques:** Writing – review & editing, Writing – original draft, Visualization, Validation, Supervision, Resources, Project administration, Methodology, Investigation, Funding acquisition, Formal analysis, Data curation, Conceptualization.

DECLARATION OF COMPETING INTEREST

The authors declare that they have no known competing financial interests or personal relationships that could have appeared to influence the work reported in this paper.

Acknowledgements

The authors thank the clinicians, Drs. Paula Sanchez Pintos (Instituto de Investigación Sanitaria Santiago de Compostela, La Coruña, Spain) and Joanna Kenny (Children's Health Ireland at Crumlin, Dublin, Ireland) for providing follow-up on the patients carrying the pathogenic variants reported in this study. This work was supported by grants PID2021-128468NB-I00 and PID2020-120258GB-I00 financed by MCIN/AEI/10.13039/501100011033 to SR-M and RF-L, respectively, and from Fundación Ramón Areces Ciencias de la Vida (XX National Call) to SR-M, and Ramon y Cajal fellowship RYC-2017-23128 to RF-L. LRM was partially supported by the FIB-HCSC intramural young researcher mobility fellowship program 2023, FIB-HCSC, Madrid, Spain. X-ray diffraction experiments at synchrotrons were done through the participation of SR-M in the BAG proposals 2023077633 at ALBA, and MX-2452 at the European Synchrotron Radiation Facility (ESRF) with DOI 10.15151/ESRF-ES-1117952942. The authors thank the ALBA and ESRF synchrotron staff for assistance during data collection.

Author contributions

FdC and SR-M conceived, planned and performed the experiments. LR-M performed MD simulations with support from LE. MM-M and RF-L contributed to the modeling and interpretation of CAD structure. All authors discussed the results and contributed to the final manuscript.

Data availability

Atomic coordinates for S1538L and S1538A mutants are deposited in the Protein Data Bank with PDB IDs: 9FS1 (S1538L bound to Ca-Asp), 9FS2 (S1538A bound to Ca-Asp) and 9FS3 (S1538A in apo form). Previously published structures used in model building and structural comparison are available in the Protein Data Bank with PDB IDs: 5G1N, 5G1O, and 5G1P for ATC and 4C6C, 4C6I, and 4C6M for DHO domains.

Appendix A. Supplementary material

Supplementary material to this article can be found online at https://doi.org/10.1016/j.jmb.2024.168832.

Received 9 September 2024;
Accepted 19 October 2024;
Available online 22 October 2024

Keywords:
pyrimidine nucleotide biosynthesis;
inborn errors of metabolisms;
pathogenic variant;
dihydroorotase;
aspartate transcarbamoylase

References

1. Del Cano-Ochoa, F., Moreno-Morcillo, M., Ramon-Maiques, S., (2019). CAD, A multienzymatic protein at the head of de novo pyrimidine biosynthesis. *Subcell. Biochem.* **93**, 505–538. https://doi.org/10.1007/978-3-030-28151-9_17.
2. Coleman, P.F., Suttle, D.P., Stark, G.R., (1977). Purification from hamster cells of the multifunctional protein that initiates de novo synthesis of pyrimidine nucleotides. *J. Biol. Chem.* **252**, 6379–6385.
3. Jones, M.E., (1980). Pyrimidine nucleotide biosynthesis in animals: genes, enzymes, and regulation of UMP biosynthesis. *Annu. Rev. Biochem* **49**, 253–279.
4. Ng, B.G., Wolfe, L.A., Ichikawa, M., Markello, T., He, M., Tifft, C.J., Gahl, W.A., Freeze, H.H., (2015). Biallelic mutations in CAD, impair de novo pyrimidine biosynthesis and decrease glycosylation precursors. *Hum. Mol. Genet.* **24**, 3050–3057. https://doi.org/10.1093/hmg/ddv057.
5. Koch, J., Mayr, J.A., Alhaddad, B., Rauscher, C., Bierau, J., Kovacs-Nagy, R., Coene, K.L.M., Bader, I., Holzhacker, M., Prokisch, H., Venselaar, H., Wevers, R.A., Distelmaier, F., Polster, T., Leiz, S., Betzler, C., Strom, T.M., Sperl, W., Meitinger, T., Wortmann, S.B., Haack, T.B., (2017). CAD mutations and uridine-responsive epileptic encephalopathy. *Brain* **140**, 279–286. https://doi.org/10.1093/brain/aww300.
6. Rymen, D., Lindhout, M., Spanou, M., Ashrafzadeh, F., Benkel, I., Betzler, C., Coubes, C., Hartmann, H., Kaplan, J.D., Ballhausen, D., Koch, J., Lotte, J., Mohammadi, M.H., Rohrbach, M., Dinopoulos, A., Wermuth, M., Willis, D., Brugger, K., Wevers, R.A., Boltshauser, E., Bierau, J., Mayr, J.A., Wortmann, S.B., (2020). Expanding the clinical and genetic spectrum of CAD deficiency: an epileptic encephalopathy treatable with uridine supplementation. *Genet. Med.* **22**, 1589–1597. https://doi.org/10.1038/s41436-020-0933-z.
7. Al-Otaibi, A., AlAyed, A., Al Madhi, A., Saeed, L., Ng, B.G., Freeze, H.H., Almannai, M., (2022). Uridine monophosphate (UMP)-responsive developmental and epileptic encephalopathy: a case report of two siblings

and a review of literature. *Mol. Genet. Metab. Rep.* **30**, https://doi.org/10.1016/j.ymgmr.2021.100835 100835.
8. Duan, L., Ye, L., Yin, R., Sun, Y., Yu, W., Zhang, Y., Zhong, H., Bao, X., Tian, X., (2024). Novel CAD gene mutations in a boy with developmental and epileptic encephalopathy 50 with dramatic response to uridine therapy: a case report and a review of the literature. *BMC Pediatr.* **24**, 160. https://doi.org/10.1186/s12887-024-04593-6.
9. Frederick, A., Sherer, K., Nguyen, L., Ali, S., Garg, A., Haas, R., Sahagian, M., Bui, J., (2021). Triacetyluridine treats epileptic encephalopathy from CAD mutations: a case report and review. *Ann. Clin. Transl. Neurol.* **8**, 284–287. https://doi.org/10.1002/acn3.51257.
10. Kamate, M., Patil, S., (2020). CAD deficiency—another treatable early infantile epileptic encephalopathy. *Pediatr. Neurol.* **110**, 97–98. https://doi.org/10.1016/j.pediatrneurol.2020.05.001.
11. McGraw, C.M., Mahida, S., Jayakar, P., Koh, H.Y., Taylor, A., Resnick, T., Rodan, L., Schwartz, M.A., Ejaz, A., Sankaran, V.G., Berry, G., Poduri, A., (2021). Uridine-responsive epileptic encephalopathy due to inherited variants in CAD: a tale of two siblings. *Ann. Clin. Transl. Neurol.* **8**, 716–722. https://doi.org/10.1002/acn3.51272.
12. Peng, X., Xia, L., Zhang, H., Zhang, J., Yu, S., Wang, S., Xu, Y., Yao, B., Ye, J., (2022). A treatable genetic disease caused by CAD mutation. *Front. Pediatr.* **10** https://doi.org/10.3389/fped.2022.771374.
13. Steinberg-Shemer, O., Yacobovich, J., Noy-Lotan, S., Dgany, O., Krasnov, T., Barg, A., Landau, Y.E., Kneller, K., Somech, R., Gilad, O., Brik Simon, D., Orenstein, N., Izraeli, S., Del Caño-Ochoa, F., Tamary, H., Ramón-Maiques, S., (2023). Biallelic hypomorphic variants in CAD cause uridine-responsive macrocytic anaemia with elevated haemoglobin-A2. *Br. J. Haematol.*. https://doi.org/10.1111/bjh.19215.
14. Yarahmadi, S.G., Morovvati, S., (2022). CAD gene and early infantile epileptic encephalopathy-50; three Iranian deceased patients and a novel mutation: case report. *BMC Pediatr.* **22**, 125. https://doi.org/10.1186/s12887-022-03195-4.
15. Zhou, L., Xu, H., Wang, T., Wu, Y., (2020). A patient with CAD deficiency responsive to uridine and lietrature review. *Front. Neurol.* **11**, 5. https://doi.org/10.3389/fneur.2020.00064.
16. Del Caño-Ochoa, F., Ramón-Maiques, S., (2021). Deciphering CAD: Structure and function of a mega-enzymatic pyrimidine factory in health and disease. *Protein Sci.* **30**, 1995–2008. https://doi.org/10.1002/pro.4158.
17. Lee, L., Kelly, R.E., Pastra-Landis, S.C., Evans, D.R., (1985). Oligomeric structure of the multifunctional protein CAD that initiates pyrimidine biosynthesis in mammalian cells. *PNAS* **82**, 6802–6806.
18. Grande-Garcia, A., Lallous, N., Diaz-Tejada, C., Ramon-Maiques, S., (2014). Structure, functional characterization, and evolution of the dihydroorotase domain of human CAD. *Structure* **22**, 185–198. https://doi.org/10.1016/j.str.2013.10.016.
19. Lallous, N., Grande-Garcia, A., Molina, R., Ramon-Maiques, S., (2012). Expression, purification, crystallization and preliminary X-ray diffraction analysis of the dihydroorotase domain of human CAD. *Acta Crystallogr.Sect. F, Struct. Biol. Crystalliz. Commun.* **68**, 1341–1345. https://doi.org/10.1107/s1744309112038857.
20. Ruiz-Ramos, A., Velazquez-Campoy, A., Grande-Garcia, A., Moreno-Morcillo, M., Ramon-Maiques, S., (2016). Structure and functional characterization of human aspartate transcarbamoylase, the target of the anti-tumoral drug PALA. *Structure* **24**, 1081–1094. https://doi.org/10.1016/j.str.2016.05.001.
21. Ruiz-Ramos, A., Lallous, N., Grande-Garcia, A., Ramon-Maiques, S., (2013). Expression, purification, crystallization and preliminary X-ray diffraction analysis of the aspartate transcarbamoylase domain of human CAD. *Acta Crystallogr. Sect. F, Struct. Biol. Crystalliz. Commun.* **69**, 1425–1430. https://doi.org/10.1107/S1744309113031114.
22. Carrey, E.A., (1995). The shape of CAD. In: Davidson, J.N. (Ed.), *Paths to Pyrimidines – An International Newsletter*. University of Kentuky, pp. 68–72.
23. Moreno-Morcillo, M., Grande-Garcia, A., Ruiz-Ramos, A., Del Cano-Ochoa, F., Boskovic, J., Ramon-Maiques, S., (2017). Structural insight into the core of CAD, the multifunctional protein leading de novo pyrimidine biosynthesis. *Structure* **25**, 912–923 e5. https://doi.org/10.1016/j.str.2017.04.012.
24. Del Caño-Ochoa, F., Ng, B.G., Abedalthagafi, M., Almannai, M., Cohn, R.D., Costain, G., Elpeleg, O., Houlden, H., Karimiani, E.G., Liu, P., Manzini, M.C., Maroofian, R., Muriello, M., Al-Otaibi, A., Patel, H., Shimon, E., Sutton, V.R., Toosi, M.B., Wolfe, L.A., Rosenfeld, J.A., Freeze, H.H., Ramón-Maiques, S., (2020). Cell-based analysis of CAD variants identifies individuals likely to benefit from uridine therapy. *Genet. Med.* **22**, 1598–1605. https://doi.org/10.1038/s41436-020-0833-2.
25. Del Caño-Ochoa, F., Ng, B.G., Rubio-del-Campo, A., Mahajan, S., Wilson, M.P., Vilar, M., Rymen, D., Sánchez-Pintos, P., Kenny, J., Ley Martos, M., Campos, T., Wortmann, S.B., Freeze, H.H., Ramón-Maiques, S., (2023). Beyond genetics: Deciphering the impact of missense variants in CAD deficiency. *J of Inher Metab Disea*, jimd.12667. https://doi.org/10.1002/jimd.12667.
26. García-Nafría, J., Watson, J.F., Greger, I.H., (2016). IVA cloning: A single-tube universal cloning system exploiting bacterial in vivo assembly. *Sci. Rep.* **6**, 27459. https://doi.org/10.1038/srep27459.
27. Del Cano-Ochoa, F., Grande-Garcia, A., Reverte-Lopez, M., D'Abramo, M., Ramon-Maiques, S., (2018). Characterization of the catalytic flexible loop in the dihydroorotase domain of the human multi-enzymatic protein CAD. *J. Biol. Chem.* **293**, 18903–18913. https://doi.org/10.1074/jbc.RA118.005494.
28. Christopherson, R.I., Jones, M.E., (1980). The overall synthesis of L-5, 6-dihydroorotate by multienzymatic protein pyr1-3 from hamster cells. Kinetic studies, substrate channeling, and the effects of inhibitors. *J. Biol. Chem.* **255**, 11381–11395.
29. Prescott, L.M., Jones, M.E., (1969). Modified methods for the determination of carbamyl aspartate. *Anal. Biochem.* **32**, 408–419.
30. Niesen, F.H., Berglund, H., Vedadi, M., (2007). The use of differential scanning fluorimetry to detect ligand interactions that promote protein stability. *Nature Protoc.* **2**, 2212–2221. https://doi.org/10.1038/nprot.2007.321.
31. Monaco, S., Gordon, E., Bowler, M.W., Delagenière, S., Guijarro, M., Spruce, D., Svensson, O., McSweeney, S.M., McCarthy, A.A., Leonard, G., Nanao, M.H., (2013). Automatic processing of macromolecular crystallography

X-ray diffraction data at the ESRF. *J. Appl. Cryst.* **46**, 804–810. https://doi.org/10.1107/S0021889813006195.
32. Vonrhein, C., Flensburg, C., Keller, P., Sharff, A., Smart, O., Paciorek, W., Womack, T., Bricogne, G., (2011). Data processing and analysis with the autoPROC toolbox. *Acta Crystallogr. D Biol. Crystallogr.* **67**, 293–302. https://doi.org/10.1107/S0907444911007773.
33. McCoy, A.J., Grosse-Kunstleve, R.W., Adams, P.D., Winn, M.D., Storoni, L.C., Read, R.J., (2007). Phaser crystallographic software. *J. Appl. Cryst.* **40**, 658–674. https://doi.org/10.1107/S0021889807021206.
34. Emsley, P., Lohkamp, B., Scott, W.G., Cowtan, K., (2010). Features and development of Coot. *Acta Crystallogr. D Biol. Crystallogr.* **66**, 486–501. https://doi.org/10.1107/S0907444910007493.
35. Adams, P.D., Afonine, P.V., Bunkoczi, G., Chen, V.B., Davis, I.W., Echols, N., Headd, J.J., Hung, L.W., Kapral, G. J., Grosse-Kunstleve, R.W., McCoy, A.J., Moriarty, N.W., Oeffner, R., Read, R.J., Richardson, D.C., Richardson, J. S., Terwilliger, T.C., Zwart, P.H., (2010). PHENIX: A comprehensive Python-based system for macromolecular structure solution. *Acta Crystallogr. D Biol. Crystallogr.* **66**, 213–221. https://doi.org/10.1107/S0907444909052925.
36. Murshudov, G.N., Skubak, P., Lebedev, A.A., Pannu, N.S., Steiner, R.A., Nicholls, R.A., Winn, M.D., Long, F., Vagin, A.A., (2011). REFMAC5 for the refinement of macromolecular crystal structures. *Acta Crystallogr. D Biol. Crystallogr.* **67**, 355–367. https://doi.org/10.1107/S0907444911001314.
37. Winn, M.D., Ballard, C.C., Cowtan, K.D., Dodson, E.J., Emsley, P., Evans, P.R., Keegan, R.M., Krissinel, E.B., Leslie, A.G., McCoy, A., McNicholas, S.J., Murshudov, G. N., Pannu, N.S., Potterton, E.A., Powell, H.R., Read, R.J., Vagin, A., Wilson, K.S., (2011). Overview of the CCP4 suite and current developments. *Acta Crystallogr. D Biol. Crystallogr.* **67**, 235–242. https://doi.org/10.1107/S0907444910045749.
38. Wyatt, P.J., (1993). Light scattering and the absolute characterization of macromolecules. *Anal. Chim. Acta* **272**, 1–40. https://doi.org/10.1016/0003-2670(93)80373-S.
39. Cheng, J., Novati, G., Pan, J., Bycroft, C., Žemgulytė, A., Applebaum, T., Pritzel, A., Wong, L.H., Zielinski, M., Sargeant, T., Schneider, R.G., Senior, A.W., Jumper, J., Hassabis, D., Kohli, P., Avsec, Ž., (2023). Accurate proteome-wide missense variant effect prediction with AlphaMissense. *Science* **381**, https://doi.org/10.1126/science.adg7492 eadg7492.
40. Schymkowitz, J., Borg, J., Stricher, F., Nys, R., Rousseau, F., Serrano, L., (2005). The FoldX web server: An online force field. *Nucleic Acids Res.* **33**, W382–W388. https://doi.org/10.1093/nar/gki387.
41. Bromberg, Y., Rost, B., (2009). Correlating protein function and stability through the analysis of single amino acid substitutions. *BMC Bioinf.* **10**, S8. https://doi.org/10.1186/1471-2105-10-S8-S8.
42. Seifi, M., Walter, M.A., (2018). Accurate prediction of functional, structural, and stability changes in PITX2 mutations using in silico bioinformatics algorithms. *PLoS One* **13**, https://doi.org/10.1371/journal.pone.0195971 e0195971.
43. Abraham, M.J., Murtola, T., Schulz, R., Páll, S., Smith, J. C., Hess, B., Lindahl, E., (2015). GROMACS: High performance molecular simulations through multi-level parallelism from laptops to supercomputers. *SoftwareX* **1–2**, 19–25. https://doi.org/10.1016/j.softx.2015.06.001.
44. Jo, S., Kim, T., Iyer, V.G., Im, W., (2008). CHARMM-GUI: A web-based graphical user interface for CHARMM. *J. Comput. Chem.* **29**, 1859–1865. https://doi.org/10.1002/jcc.20945.
45. Huang, J., Rauscher, S., Nawrocki, G., Ran, T., Feig, M., de Groot, B.L., Grubmüller, H., MacKerell, A.D., (2017). CHARMM36m: An improved force field for folded and intrinsically disordered proteins. *Nature Methods* **14**, 71–73. https://doi.org/10.1038/nmeth.4067.
46. Croitoru, A., Park, S.-J., Kumar, A., Lee, J., Im, W., Jr, A. D., MacKerell, A.A., (2021). Additive CHARMM36 force field for nonstandard amino acids. *J. Chem. Theory Comput.* **17**, 3554–3570. https://doi.org/10.1021/acs.jctc.1c00254.
47. Darden, T., Tork, D., Pedersen, L., (1997). Particle mesh Ewald: An N-log(N) method for Ewald sums in large systems. *J. Comput. Chem.* **18**, 1463–1472.
48. Hunter, J., (2007). Matplotlib: A 2D graphics environment. *Comput. Sci. Eng.* **9**, 90–95.
49. Pettersen, E.F., Goddard, T.D., Huang, C.C., Couch, G.S., Greenblatt, D.M., Meng, E.C., Ferrin, T.E., (2004). UCSF Chimera–A visualization system for exploratory research and analysis. *J. Comput. Chem.* **25**, 1605–1612. https://doi.org/10.1002/jcc.20084.
50. Collins, K.D., Stark, G.R., (1971). Aspartate transcarbamylase interaction with the transition state analogue N-(phosphonacetyl)-L-aspartate. *J. Biol. Chem.* **246**, 6599–6605.
51. Henzler-Wildman, K., Kern, D., (2007). Dynamic personalities of proteins. *Nature* **450**, 964–972. https://doi.org/10.1038/nature06522.
52. Jumper, J., Evans, R., Pritzel, A., Green, T., Figurnov, M., Ronneberger, O., Tunyasuvunakool, K., Bates, R., Žídek, A., Potapenko, A., Bridgland, A., Meyer, C., Kohl, S.A.A., Ballard, A.J., Cowie, A., Romera-Paredes, B., Nikolov, S., Jain, R., Adler, J., Back, T., Petersen, S., Reiman, D., Clancy, E., Zielinski, M., Steinegger, M., Pacholska, M., Berghammer, T., Bodenstein, S., Silver, D., Vinyals, O., Senior, A.W., Kavukcuoglu, K., Kohli, P., Hassabis, D., (2021). Highly accurate protein structure prediction with AlphaFold. *Nature* **596**, 583–589. https://doi.org/10.1038/s41586-021-03819-2.
53. Thoden, J.B., Holden, H.M., Wesenberg, G., Raushel, F. M., Rayment, I., (1997). Structure of carbamoyl phosphate synthetase: a journey of 96 A from substrate to product. *Biochemistry* **36**, 6305–6316. https://doi.org/10.1021/bi970503q.
54. de Cima, S., Polo, L.M., Diez-Fernandez, C., Martinez, A.I., Cervera, J., Fita, I., Rubio, V., (2015). Structure of human carbamoyl phosphate synthetase: Deciphering the on/off switch of human ureagenesis. *Sci. Rep.* **5**, 16950. https://doi.org/10.1038/srep16950.
55. Otsuki, T., Mori, M., Tatibana, M., (1982). Studies on channeling of carbamoyl-phosphate in the multienzyme complex that initiates pyrimidine biosynthesis in rat ascites hepatoma cells. *J. Biochem.* **92**, 1431–1437.
56. Mally, M.I., Grayson, D.R., Evans, D.R., (1980). Catalytic synergy in the multifunctional protein that initiates pyrimidine biosynthesis in Syrian hamster cells. *J. Biol. Chem.* **255**, 11372–11380.
57. Carrey, E.A., Campbell, D.G., Hardie, D.G., (1985). Phosphorylation and activation of hamster carbamyl

phosphate synthetase II by cAMP-dependent protein kinase. A novel mechanism for regulation of pyrimidine nucleotide biosynthesis. *EMBO J.* **4**, 3735.
58. Ben-Sahra, I., Howell, J.J., Asara, J.M., Manning, B.D., (2013). Stimulation of de novo pyrimidine synthesis by growth signaling through mTOR and S6K1. *Science* **339**, 1323–1328. https://doi.org/10.1126/science.1228792.
59. Robitaille, A.M., Christen, S., Shimobayashi, M., Cornu, M., Fava, L.L., Moes, S., Prescianotto-Baschong, C., Sauer, U., Jenoe, P., Hall, M.N., (2013). Quantitative phosphoproteomics reveal mTORC1 activates de novo pyrimidine synthesis. *Science* **339**, 1320–1323. https://doi.org/10.1126/science.1228771.
60. Graves, L.M., Guy, H.I., Kozlowski, P., Huang, M., Lazarowski, E., Pope, R.M., Collins, M.A., Dahlstrand, E. N., Earp, H.S., Evans, D.R., (2000). Regulation of carbamoyl phosphate synthetase by MAP kinase. *Nature* **403**, 328–332. https://doi.org/10.1038/35002111.
61. Yang, C., Zhao, Y., Wang, L., Guo, Z., Ma, L., Yang, R., Wu, Y., Li, X., Niu, J., Chu, Q., Fu, Y., Li, B., (2023). De novo pyrimidine biosynthetic complexes support cancer cell proliferation and ferroptosis defence. *Nature Cell Biol.* **25**, 836–847. https://doi.org/10.1038/s41556-023-01146-4.
62. Qiu, Y., Davidson, J.N., (2000). Substitutions in the aspartate transcarbamoylase domain of hamster CAD disrupt oligomeric structure. *PNAS* **97**, 97–102.
63. Qiu, Y., Davidson, J.N., (1998). Aspartate-90 and arginine-269 of hamster aspartate transcarbamylase affect the oligomeric state of a chimaeric protein with an *Escherichia coli* maltose-binding domain. *Biochem. J.* **329** (Pt 2), 243–247.
64. Davidson, J.N., Rumsby, P.C., Tamaren, J., (1981). Organization of a multifunctional protein in pyrimidine biosynthesis. Analyses of active, tryptic fragments. *J. Biol. Chem.* **256**, 5220–5225.
65. Souciet, J.L., Nagy, M., Le Gouar, M., Lacroute, F., Potier, S., (1989). Organization of the yeast URA2 gene: identification of a defective dihydroorotase-like domain in the multifunctional carbamoylphosphate synthetase-aspartate transcarbamylase complex. *Gene* **79**, 59–70.
66. Lee, M., Maher, M.J., Christopherson, R.I., Guss, J.M., (2007). Kinetic and structural analysis of mutant *Escherichia coli* dihydroorotases: a flexible loop stabilizes the transition state. *Biochemistry* **46**, 10538–10550. https://doi.org/10.1021/bi701098e.
67. Lee, M., Chan, C.W., Mitchell Guss, J., Christopherson, R. I., Maher, M.J., (2005). Dihydroorotase from *Escherichia coli*: loop movement and cooperativity between subunits. *J. Mol. Biol.* **348**, 523–533. https://doi.org/10.1016/j.jmb.2005.01.067.
68. Russo, R., Marra, R., Andolfo, I., Manna, F., Rosa, G.D., Rosato, B.E., Radhakrishnan, K., Fahey, M., Iolascon, A., (2020). Uridine treatment normalizes the congenital dyserythropoietic anemia type II-like hematological phenotype in a patient with homozygous mutation in the CAD gene. *Am. J. Hematol.* **95**, 1423–1426. https://doi.org/10.1002/ajh.25946.